PHYSICAL REVIEW B **109**, 035112 (2024)

Conductive surface states and Kondo exhaustion in insulating $YbIr_3Si_7$

Macy Stavinoha,[1] C.-L. Huang,[2] W. Adam Phelan,[3] Alannah M. Hallas,[2,4,5] V. Loganathan,[2] M. Michiardi,[4,5,6] J. Falke,[6] Sergey Zhdanovich,[4,5] D. Takegami,[6] C.-E. Liu,[6] K. D. Tsuei,[7] C. T. Chen,[7] Long Qian,[1] Nicholas J. Ng,[8] Jeffrey W. Lynn,[9] Qingzhen Huang,[9] Franziska Weickert,[10] Vivien Zapf,[10] Katharine R. Larsen,[11] Patricia D. Sparks,[11] James C. Eckert,[11] Anand B. Puthirath,[12] Hsiang-Hsi Kung,[4,5] Tor M. Pedersen,[13] Sergey Gorovikov,[13] A. Damascelli,[4,5] L. H. Tjeng,[6] C. Hooley,[14] Andriy H. Nevidomskyy,[2] and E. Morosan[1,2]

[1] *Department of Chemistry, Rice University, Houston, Texas 77005, USA*
[2] *Department of Physics and Astronomy, Rice University, Houston, Texas 77005, USA*
[3] *Los Alamos National Laboratory, Los Alamos, New Mexico 87545, USA*
[4] *Department of Physics & Astronomy, University of British Columbia, Vancouver, Canada BC V6T 1Z1*
[5] *Quantum Matter Institute, University of British Columbia, Vancouver, Canada BC V6T 1Z4*
[6] *Max Planck Institute for Chemical Physics of Solids, Nöthnitzer Straße 40, 01187 Dresden, Germany*
[7] *National Synchrotron Radiation Research Center (NSRRC), 101 Hsin-Ann Road, 30076 Hsinchu, Taiwan, Republic of China*
[8] *Platform for the Accelerated Realization, Analysis, and Discovery of Interface Materials (PARADIM), Department of Chemistry, The Johns Hopkins University, Baltimore, Maryland 21218, USA*
[9] *NIST Center for Neutron Research, National Institute of Standards and Technology, Gaithersburg, Maryland 20899, USA*
[10] *National High Magnetic Field Laboratory, Materials Physics and Applications Division, Los Alamos National Laboratory, Los Alamos, New Mexico 87545, USA*
[11] *Department of Physics, Harvey Mudd College, Claremont, California 91711, USA*
[12] *Department of Materials Science and NanoEngineering, Rice University, Houston, Texas 77005, USA*
[13] *Canadian Light Source, Inc., 44 Innovation Boulevard, Saskatoon, Canada SK S7N 2V3*
[14] *Scottish Universities Physics Alliance, School of Physics and Astronomy, University of St. Andrews, North Haugh, St. Andrews, Fife KY16 9SS, United Kingdom*

(Received 9 August 2023; revised 1 November 2023; accepted 3 November 2023; published 8 January 2024)

The interplay of Kondo screening and magnetic ordering in strongly correlated materials containing local moments is a subtle problem. Usually the number of conduction electrons per unit cell matches or exceeds the number of moments, and a Kondo-screened heavy Fermi liquid develops at low temperatures. Changing the pressure, magnetic field, or chemical doping can displace this heavy Fermi liquid in favor of a magnetically ordered state. Alternatively, Kondo singlet formation can be suppressed when the number of conduction electrons is small compared to the number of magnetic moments, known as the Kondo exhaustion scenario. Here we report the discovery of such an "exhausted" Kondo lattice material, $YbIr_3Si_7$, where the *bulk* electrical conductivity tends to zero in the antiferromagnetic state below the Néel temperature $T_N = 4.1$ K, as all the free carriers are consumed in the formation of Kondo singlets. By contrast, the *surface* is conducting, as the Yb^{3+} ions relax into larger nonmagnetic Yb^{2+} in the presence of reduced chemical pressure, which shifts the chemical potential.

DOI: 10.1103/PhysRevB.109.035112

I. INTRODUCTION

Kondo materials based on localized f electrons offer a rich playground for the interplay of magnetic order on the one hand, and the Kondo screening of magnetic moments by conduction (c) electrons on the other. When compared to these Kondo metals, the new system reported here, $YbIr_3Si_7$, has two distinct properties. First, $YbIr_3Si_7$ orders antiferromagnetically below its Néel temperature $T_N = 4.1$ K against the backdrop of insulating bulk resistivity onsetting at much higher temperatures ($\gtrsim$50 K). Second, $YbIr_3Si_7$ displays conducting surface states, contrasting with its insulating bulk properties. Through a combination of bulk- and surface-sensitive transport and spectroscopic measurements, and density functional calculations, we propose Kondo exhaustion as a scenario that accounts for both of these observations in $YbIr_3Si_7$.

II. RESULTS

Single crystals of $YbIr_3Si_7$ were grown using the laser pedestal technique. Details of the crystallographic structure and growth are included in Appendix A. Figure 1(a) shows the $H = 0$ electrical resistivity $\rho(T)$ of $YbIr_3Si_7$ (symbols), indicative of insulating behavior. The data for the nonmagnetic analog $LuIr_3Si_7$ (dashed line), where $\rho(T)$ is weakly T-dependent and overall very large ($\sim 10^{-2}$ Ω cm), suggest large disorder scattering, low-carrier density, or a combination of both in the RIr_3Si_7 ($R =$ Yb,Lu) material class, and this will be reexamined below in the context of Hall measurements and density functional theory (DFT) calculations. A striking feature is that the $YbIr_3Si_7$ resistivity increases by ~4 orders of magnitude on cooling from 300 to 0.3 K. At low T, the resistivity levels off [Fig. 1(a)]. On the way to the low-temperature plateau, two notable features occur in

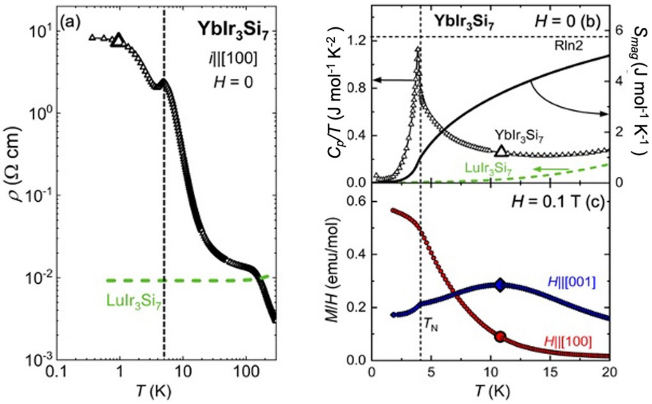

FIG. 1. (a) $H = 0$ temperature-dependent resistivity for $\mathrm{YbIr_3Si_7}$ single crystals (open triangles) and the polycrystalline nonmagnetic analog $\mathrm{LuIr_3Si_7}$ (dashed line). (b) $H = 0$ specific heat scaled by temperature C_p/T (left axis) for $\mathrm{YbIr_3Si_7}$ (symbols) and $\mathrm{LuIr_3Si_7}$ (dashed line). Right axis: $\mathrm{YbIr_3Si_7}$ magnetic entropy S_{mag} (solid line). (c) Low-temperature magnetic susceptibility M/H for $\mu_0 H =$ 0.1 T along $H \parallel [100]$ (red circles) and $H \parallel [001]$ (blue diamonds). Vertical dashed lines mark the antiferromagnetic ordering temperature T_{N}.

$\rho(T)$ for $\mathrm{YbIr_3Si_7}$, around 100 and 5 K. The high-temperature feature does not have a magnetic component as it does not change from $\mu_0 H = 0$ to 9 T (Fig. 7 in Appendix B). Inelastic neutron scattering measurements (Fig. 9, Appendix B) suggest that the crystal electric field (CEF) may not be the dominant effect at this temperature, even though CEF effects cannot be uniquely resolved from transport data: the lowest CEF level was measured at 19 meV (~200 K), higher than the $\rho(T)$ feature, and the scattering did not change between measurements performed at 10 and 150 K. Furthermore, the same high-temperature feature in $\rho(T)$ (around 100 K) disappears in the dilute moment limit, as demonstrated by the resistivity measurements on $\mathrm{Yb_{0.05}Lu_{0.95}Ir_3Si_7}$ (Fig. 8 in Appendix B), when a single-ion CEF feature should be independent of the concentration on magnetic ions. Lastly, a structural phase transition can also be excluded since neutron diffraction data at $T = 1.5$ K (shown below) confirm the room-temperature structure and space group. We conclude that the 100 K resistivity feature could be due to the onset of Kondo correlations, alone or in combination with CEF effects.

On further cooling, the resistivity increase does not appear to follow the Arrhenius activation temperature dependence, but instead is better described by a power law (Fig. 7 in Appendix B). As thermodynamic measurements [Figs. 1(b) and 1(c)] and neutron scattering (below) reveal, antiferromagnetic long-range order sets in at $T_{\mathrm{N}} = 4.1$ K. Zero-field specific-heat C_p/T data [symbols, Fig. 1(b)] show a peak at 4.1 K, while the nonmagnetic analog $\mathrm{LuIr_3Si_7}$ (dashed line) displays much smaller C_p/T values and no phase transition. Above the ordering temperature, a large tail in the $\mathrm{YbIr_3Si_7}$ specific heat could be the result of short-range magnetic interactions. The magnetic entropy S_{mag} for $\mathrm{YbIr_3Si_7}$ [solid line, Fig. 1(b)] was estimated from $S_{\mathrm{mag}} = \int_0^T \frac{C_{\mathrm{mag}}}{T}\, dT$, where $C_{\mathrm{mag}} = C_p(\mathrm{YbIr_3Si_7}) - C_p(\mathrm{LuIr_3Si_7})$. At T_{N}, the low entropy release of ~15% $R\ln 2$ signals Kondo screening, with an estimated Kondo temperature $T_{\mathrm{K}} \approx 15$ K from $S_{\mathrm{mag}}(0.5\,T_{\mathrm{K}}) = 0.5\,R\ln 2$. With this T_{K} estimate in mind, the inflection in the $H = 0\,\mathrm{YbIr_3Si_7}$ resistivity data just above T_N [Fig. 1(a)] is coincident with T_K.

Further confirmation of the long-range magnetic order is provided through anisotropic magnetic susceptibility measurements M/H shown in Fig. 1(c). Temperature-dependent M/H measurements with $\mu_0 H = 0.1$ T confirm the magnetic phase transition since small inflections are observed on cooling for both $H \parallel [100]$ (circles) and $H \parallel [001]$ (diamonds). On warming above T_{N}, the $H \parallel [001]$ data [full diamonds in Fig. 1(c)] display a broad maximum centered around 10 K, while a similar feature at 10 K is absent in the [100] field orientation. The crossing of the anisotropic M/H curves just above T_{N} is reminiscent of the hard axis ordering observed in both known isostructural Yb systems $\mathrm{YbIr_3Ge_7}$ [1], $\mathrm{YbRh_3Si_7}$ [2], and in the few other known FM Kondo lattice compounds [3]. Indeed, the susceptibility at high temperatures (Fig. 10 in Appendix B) is indicative of large crystal electric field anisotropy favoring a [001] easy axis. The average magnetization M_{ave} was calculated using $M_{\mathrm{ave}} = \frac{1}{3}(2M_{100} + M_{001})$. A linear fit to the average inverse susceptibility at high temperatures (above 150 K) yields an effective moment $\mu_{\mathrm{eff}} = 4.42\mu_B$, which is slightly smaller the theoretical value of $4.54\mu_B$ for $\mathrm{Yb^{3+}}$, consistent with the HAXPES estimate below [Fig. 3(a)].

Altogether, specific heat and magnetic susceptibility measurements [Figs. 1(b) and 1(c) and Fig. 10] support the nearly 3+ valence of Yb, while bringing solid evidence for the bulk Kondo screening, and providing an estimate of the Kondo temperature. The onset of this order appears to momentarily interrupt the $\rho(T)$ divergence [Fig. 1(a)]. We interpret this as the temporary "liberation" of free carriers as the magnetic moments emerge from their screening clouds to form the Néel state. However, contrary to the usual behavior for $T \ll T_{\mathrm{N}}$, the resistivity then resumes its rise upon further cooling before it plateaus at the lowest temperatures.

The low-temperature resistivity plateau in $\mathrm{YbIr_3Si_7}$ prompts an inquiry into its origin, which could be rooted in a more conductive surface compared to the bulk. We therefore turn our attention to the characterization of the electronic properties of the surface. First, the resistivity ρ as a function of sample thickness d [Fig. 2(a)] reveals that the relative sample surface (conductive)-to-bulk volume (insulating) ratio increases when the thickness decreases, and should result in an overall resistivity ρ decrease. The inset of Fig. 2(a) confirms that the low-T resistivity decreases as the crystal is thinned from 723 to 77 µm. The insulating bulk dominates the resistivity above 453 µm (black), but for thinner samples the low T resistivity drops by an order of magnitude.

Hall effect measurements for the magnetic $\mathrm{YbIr_3Si_7}$ (triangles) and its nonmagnetic analog $\mathrm{LuIr_3Si_7}$ (squares) are shown in Fig. 2(b). For $\mathrm{YbIr_3Si_7}$, the initial Hall coefficient R_{H} (in the zero-field limit) increases by an order of the magnitude on cooling from 300 K ($\sim 0.4 \times 10^{-6}$ m^3/C) to 2 K ($\sim 4 \times 10^{-6}$ m^3/C) [Fig. 2(b)], suggesting an order-of-magnitude decrease of the carrier density. Conversely, the Hall coefficient for $\mathrm{LuIr_3Si_7}$, R_{H}, is much smaller and shows only a small temperature dependence, dwelling around 0.03×10^{-6} m^3/C [Fig. 2(b)] for the entire temperature range. The dimensions for all samples in this measurement set are listed in Table II.

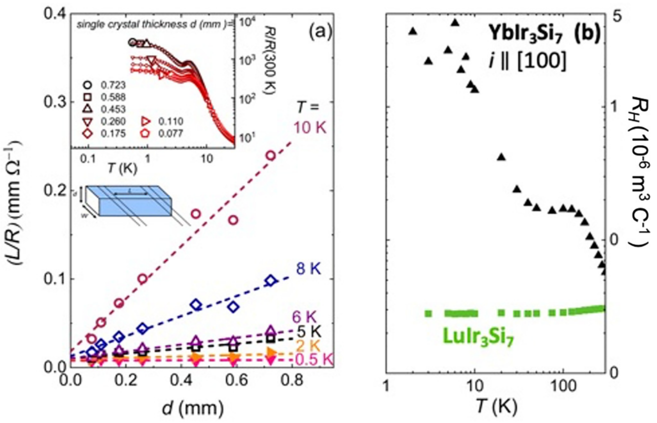

FIG. 2. (a) Inverse total resistance $1/R$, scaled by the geometric factor L, as a function of thickness d for different temperatures (see the text). Inset: $H = 0$ scaled temperature-dependent $\rho(T)$ for different thickness values d of a thinned crystal. (b) Hall coefficient R_H for $YbIr_3Si_7$ (triangles) and the nonmagnetic analog $LuIr_3Si_7$ (squares).

DFT calculations show the number of conduction carriers (not counting the ordered Yb moments) to be $3.2 \times 10^{19}/cm^3$, somewhat larger than the experimentally deduced value at 300 K, with the discrepancy perhaps to do with the approximate nature of using the single-band model. To put this in perspective, the DFT carrier density corresponds to about 2.5% electrons (and an equal number of holes) per formula unit. Such a small amount of electrons per formula unit would indeed open up the possibility that a Kondo exhaustion mechanism reduced effectively the carrier concentration at low temperatures.

To understand the reason for the low carrier concentration as well as its role in the framework of Kondo screening in $YbIr_3Si_7$, we need to look more closely into the Yb valence, beyond the initial estimate of ~3+ from the magnetic susceptibility (Fig. 10). One of the most powerful experimental methods to determine the valence is core-level photoelectron spectroscopy (PES). Due to the strong Coulomb interaction of the $4f$ electrons with the core hole, the photoemission spectra of Yb^{3+} and Yb^{2+} configurations produce peaks at distinct energies.

Figure 3(a) shows the Yb $3d$ core-level photoemission spectrum of $YbIr_3Si_7$. The data were collected using hard x-rays with an estimated probing depth of about 100 Å [4], ensuring bulk sensitivity. The experimental details are presented in Appendix D. We clearly observe the presence of both Yb^{3+} and Yb^{2+} configurations. Their identification is based on the spectral line shape, which is very specific for the two configurations, due to their characteristic atomic multiplet structures [5]. The valence can be estimated in a straightforward manner [6] and is given by

$$3 - \frac{I_{2+}}{I_{3+} + I_{2+}} = 2.94+,$$

where I_{3+} and I_{2+} are the integrated intensities for Yb^{3+} and Yb^{2+} [Fig. 3(a)]. We can expect that the valence will be lower

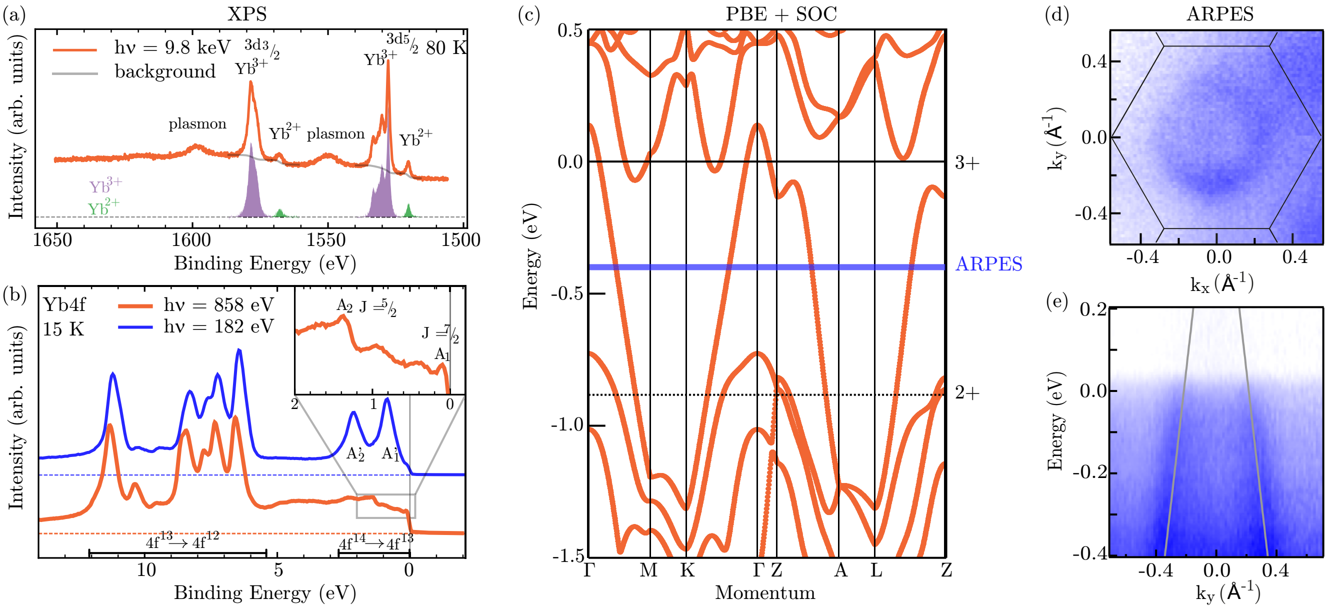

FIG. 3. (a) Yb $3d$ core-level spectrum measured using bulk-sensitive hard-x-ray PES. The Yb^{3+} and Yb^{2+} contributions (purple and green shaded areas) were extracted after substraction of the integral background, as indicated by the solid gray lines. (b) Valence-band spectra measured using bulk-sensitive PES ($h\nu = 858$ eV, orange) and surface-sensitive PES ($h\nu = 182$ eV, blue). The inset shows the Yb^{2+} contribution characterized by the spin-orbit-split $4f^{13}_{7/2,5/2}$ peaks, labeled as A_1 and A_2. The same states at the surface are shifted to 0.9 eV higher binding energy and are marked as $A'_{1,2}$. (c) Band-structure calculations of $YbIr_3Si_7$ using PBE + SOC and imposing a Yb^{3+} valence; Yb f electrons are pushed into the core for the sake of clarity. The chemical potential for the same calculation imposing Yb^{2+} valence, and as obtained from a comparison with ARPES, is also shown. (d) ARPES Fermi surface of $YbIr_3Si_7$ as measured by surface-sensitive ARPES with 88 eV photons. (e) The ARPES dispersion along the Γ-M direction is characterized by a single holelike band crossing the Fermi level. The calculated dispersion is shown as a solid gray line, and it is rigidly shifted in energy to match the ARPES Fermi level.

at lower temperatures, because Yb^{2+} has lower entropy than Yb^{3+}. The amount of change will, however, be minimal since the valence is quite close to integer [7]. We would like to note that the small amount of Yb^{2+} is consistent with the low Kondo temperature of about 15 K determined from transport [Fig. 1(a)].

We have also carried out PES measurements to study the valence band (see Appendix D). Figure 3(b) displays the valence-band spectra obtained at 858 and 182 eV. We can clearly observe the characteristic multiplet structure of the $4f^{12}$ final states originating from the Yb^{3+} $4f^{13}$ configuration [5]. We can also identify the characteristic spin-orbit-split $4f^{13}_{5/2,7/2}$ final-state peaks originating from the Yb^{2+} $4f^{14}$ configuration. These peaks are labeled A_1 and A_2 in the inset. In the 858 eV spectrum, measured with an estimated probing depth of about 20 Å [4] (much smaller than one Yb surface layer thickness of about 3 Å), the intensities of A_1 and A_2 are small. This is fully consistent with the results from the $3d$ core-level data. Analogous to other Yb-based Kondo materials systems, the low-energy peak A_1 close to the Fermi level can be identified as the Kondo resonance [8]. The low photon energy data ($h\nu = 182$ eV) reflect the higher surface sensitivity of the photoemission process, due to the shorter mean free path of about 5–8 Å [4] of the photoelectrons in this energy range. The strongly enhanced peaks marked as A_1' and A_2' correspond to the same $4f^{13}$ final states at the surface, which are now located at approximately 0.9 eV higher binding energy due to a chemical shift. The area of the 2+ peaks is comparable to the 3+ peaks, indicating an overall lower valence at the surface, which is commonly observed for Yb compounds [8–11].

To estimate the surface valence and understand the surface metallicity, we compare photoemission data to DFT calculations. The calculated open-core band structure of $\mathrm{YbIr_3Si_7}$ is shown in Fig. 3(c), where a 3+ valence for Yb is imposed. In this configuration, $\mathrm{YbIr_3Si_7}$ is a low carrier density semimetal. The chemical potential cuts through shallow hole and electron pockets. Enforcing the Yb valence to be 2+ in a rigid band fashion has the simple effect of shifting the chemical potential deeper in the holelike bands, establishing a fully metallic state in $\mathrm{YbIr_3Si_7}$. To probe the electronic structure at the surface, we measure ARPES data using 88 eV photons, i.e., probing a depth of no more than 5–8 Å [4]. Our results presented in Figs. 3(d) and 3(e) reveal a single holelike band crossing the Fermi level, which gives rise to a circular Fermi contour. The existence of this large Fermi surface confirms that the *surface* of $\mathrm{YbIr_3Si_7}$ is metallic, as suggested by the resistivity measurements in Fig. 2. Comparing the size of the measured Fermi surface with the density functional theory (DFT) calculation, we can extrapolate the position of the Fermi energy at the surface as compared to the bulk (Yb^{3+} Fermi level). As shown in Fig. 3(c), the surface Fermi level falls partway between a full Yb^{3+} and Yb^{2+} configuration.

The use of photoemission probes with different depth sensitivity allows us to determine that the difference between bulk vs surface resistivity is caused by a progression of the Yb valence from 3+ in the bulk to 2+ on the surface. The insulating state in the bulk is facilitated by the low carrier density and induced by Kondo screening. The associated singlet $4f^{14}$ state can then be used as the starting wave function to span the Hilbert space, which involves $4f^{13}$ states that are coupled to an electron in the conduction band with the appropriate symmetry, out of which the Kondo state can be formed [12]. Indeed, our bulk-sensitive PES data show this is the case in $\mathrm{YbIr_3Si_7}$.

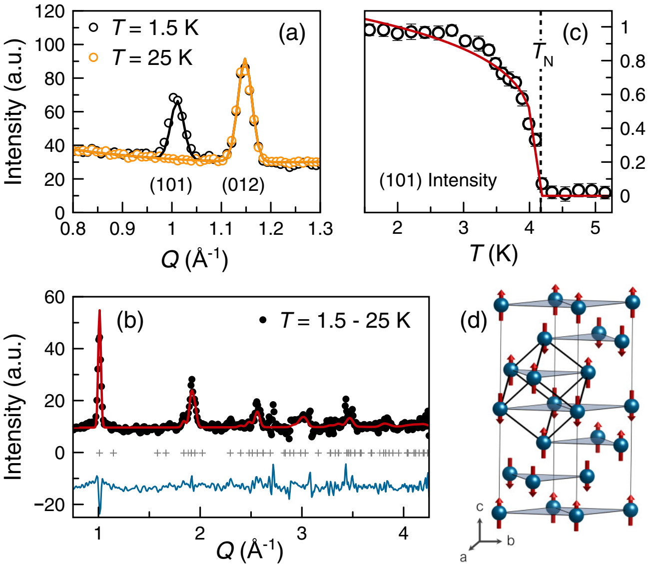

FIG. 4. (a) Powder neutron diffraction measurements for $\mathrm{YbIr_3Si_7}$ at $T = 25$ K (orange symbols) and $T = 1.5$ K (black symbols). (b) Rietveld refinement (red line) with the $k = 0$ Γ_1 irreducible representation of the magnetic diffraction pattern (black symbols), which is obtained by subtracting the $T = 25$ K from the $T = 1.5$ K data. The difference between experiment and refinement is given by the blue line and the symmetry-allowed peak positions for the $R\bar{3}c$ space group are given by the crosses. (c) Neutron order parameter from the intensity of the (101) magnetic Bragg peak. (d) The spin configuration of the Yb^{3+} moments in the Γ_1 ordered state.

To elucidate the nature of the magnetic ground state, we performed powder neutron diffraction measurements. Upon cooling from 25 K [orange symbols, Fig. 4(a)] to 1.5 K [black symbols, Fig. 4(a)], we observe the formation of magnetic Bragg peaks, which can be indexed with the propagation vector $k = 0$. There are three possible $k = 0$ irreducible representations (Γ_1, Γ_3, and Γ_5) for Yb^{3+} sitting at the $6b$ Wyckoff site within the $R\bar{3}c$ space group. The latter two of these possible magnetic structures can be ruled out, since they would generate intense magnetic Bragg peaks at positions where no peaks are observed in experiment. We are left to consider only the Γ_1 irreducible representation, and the Rietveld refinement with this magnetic structure is shown in Fig. 4(b). The magnetic diffraction pattern was isolated by subtracting a data set collected at $T = 25$ K from a data set collected at $T = 1.5$ K. This gives excellent agreement between the refinement [red line in Fig. 4(b)] and the measured data (black symbols). Furthermore, the order parameter [Fig. 4(c)], which is derived by fitting the intensity of the (101) magnetic Bragg peak, drops to 0 at $T_\mathrm{N} = 4.1$ K, consistent with the thermodynamic data [Figs. 1(b) and 1(c)]. In the Γ_1 antiferromagnetically ordered state [Fig. 4(d)], all the Yb^{3+} moments are oriented along the crystallographic c axis ([001]). Each Yb^{3+} moment is aligned antiparallel with its six nearest neighbors in the nearly cubic Yb sublattice [outlined in Fig. 4(d)], and parallel with its coplanar next nearest neighbors (gray sheets). The refined ordered moment is $1.51(5)\mu_B/\mathrm{Yb}^{3+}$.

III. DISCUSSION

Unlike many Yb-based intermetallics, or even the isostructural heavy fermions $\mathrm{YbRh_3Si_7}$ [2] or $\mathrm{YbIr_3Ge_7}$ [1], $\mathrm{YbIr_3Si_7}$ shows insulating behavior in electrical transport, albeit without evidence for a band gap (no Arrhenius divergence). On the contrary, PES, ARPES measurements, and DFT calculations establish the semimetallic nature of $\mathrm{YbIr_3Si_7}$, and at the same time indicate a valence transition from magnetic Yb^{3+} in the bulk to nonmagnetic Yb^{2+} on the surface. Recently, we demonstrated the existence of charge-neutral fermions in $\mathrm{YbIr_3Si_7}$, closely related to its magnetic ground state [13]. We look for a plausible scenario to reconcile the magnetic and electronic properties of $\mathrm{YbIr_3Si_7}$ on the backdrop of Kondo physics and strong correlations in this compound: the carrier concentration in $\mathrm{YbIr_3Si_7}$ appears smaller ($\sim 10^{19}$ cm^{-3}) than a conventional metal, and a couple of orders of magnitude smaller than in the nonmagnetic analog $\mathrm{LuIr_3Si_7}$. Moreover, the carrier concentration in the Yb compound decreases by an order of magnitude on cooling from room temperature through the magnetic order around 4 K. DFT estimates the number of carriers to account for only a small fraction of the ordered Yb^{3+} moments ($\leqslant 5\%$), suggesting a Kondo exhaustion scenario as a likely account for the observed transport in $\mathrm{YbIr_3Si_7}$. Indeed, Kondo exhaustion was proposed by Meyers and Nolte [14] for a periodic Anderson model. In $\mathrm{YbIr_3Si_7}$, the Yb valence estimated from PES is 2.94, a necessary even if not sufficient condition for Kondo exhaustion in the Anderson impurity limit. One additional observation renders support to the same exhaustion scenario, when we consider the resistivity behavior below T_N: the continued renormalization of the conductivity in the magnetically ordered state suggests that not enough carriers are left for screening the remaining nonordered fraction of each local moment. However, it is noteworthy that the Meyers and Nolte calculation [14] does not account for magnetic order. In the absence of the Kondo effect, $RT_3\mathrm{Si_7}$ (R = rare earth, T = Co, Rh) [15,16] show entangled electronic and magnetic degrees of freedom, but they lack some of the complexity (e.g., the hard axis magnetic order, spin flop transitions) that seems to emerge only when Kondo is competing with CEF and RKKY effects.

We recently reported on the distinct magnetic properties of the isostructural compounds $\mathrm{Yb}T_3M_7$ (T = Co, Rh, Ir; M = Si, Ge) [17] from other Yb-based Kondo systems [17]. The Yb-Yb distance changed very little with the different T or M in $\mathrm{Yb}T_3M_7$ (see Ref. [17] and Fig. 1 therein), implying minute or no chemical pressure. However, the ordering temperature changes by nearly an order of magnitude, while the ground state also changes between AFM and FM. However, all of the Kondo $\mathrm{Yb}T_3M_7$ compounds, except $\mathrm{YbIr_3Si_7}$, and the non-Kondo counterparts $R\mathrm{Rh_3Si_7}$ [15] are metals. It is likely that spin-orbit coupling (SOC) is at play and related to the insulating behavior in $\mathrm{YbIr_3Si_7}$, although this should be comparable with the SOC in the related FM heavy fermion $\mathrm{YbIr_3Ge_7}$ [1]. To get to the root of this question, a study is underway to compare the transport properties of the lattice, i.e., of the nonmagnetic (non-Kondo) analogs $\mathrm{Lu}T_3M_7$.

The insulating behavior in $\mathrm{YbIr_3Si_7}$ is unique not only compared to the isostructural Kondo systems $\mathrm{YbRh_3Si_7}$ [2] and $\mathrm{YbIr_3Ge_7}$ [1], but also by comparison with other known Kondo insulators or semimetals: β-$\mathrm{YbAlB_4}$ [18] is a mixed valence heavy fermion showing a metal-to-insulator transition with Mn doping; the $\mathrm{YbB_{12}}$ Kondo insulator is distinct from $\mathrm{SmB_6}$, where bulk small heavy Fermi surface signatures appear in the former, by contrast to a large light Fermi surface in the latter. In several Ce-based Kondo systems, insulating or semimetallic behavior is observed (CeNiSn, CeRhAs, $\mathrm{CeRu_4Sn_6}$) [19], where even leveling off of the low-T resistivity is observed, similar to what we observe in $\mathrm{YbIr_3Si_7}$. However, the overall transport properties cannot be fully described by any proposed theoretical models (increased disorder with doping, two gap structure model, etc.). While the valence change and surface effects have not been explored in these Kondo systems, the scenario we propose for $\mathrm{YbIr_3Si_7}$ would not work the same way for the Ce compounds, where the low-T resistivity plateau is observed: in Yb compounds, Yb^{3+} (smaller) relaxes at the surface to the Yb^{2+} (larger) state. However, the magnetic Ce^{3+} ion is smaller in size than the nonmagnetic Ce^{4+}, and therefore a valence transition would be unstable at the surface in Ce Kondo systems.

Valence transitions have been observed in a few bulk materials, including the doped fullerides $(\mathrm{Sm_{1/3}Ca_{2/3}})_{2.75}\mathrm{C_{60}}$ [20], $\mathrm{EuRh_2Si_2}$ [21], and $\mathrm{YbNi_3Ga_9}$ [22]. In all of these compounds, large pressures were required ($\sim$1–9 GPa) to induce the valence transition in the bulk, revealing possibly coupled lattice and electronic degrees of freedom. Surface valence transitions have been reported in insulating $\mathrm{EuF_3}$, $\mathrm{Eu_2O_3}$, and $\mathrm{EuCl_3}$ [23], while in metallic compounds ($\mathrm{YbIn_2}$, $\mathrm{Yb_4As_3}$, $\mathrm{YbCu_2}$, $\mathrm{YbAl_3}$, $\mathrm{Yb_4Sb_3}$, $\mathrm{Yb_4Bi_3}$) the electronic structure at the surface changes compared to bulk due to a surface core-level shift [24]. However, no Kondo physics is at play in these insulating Eu compounds, where a trivalent to divalent Eu transition is evidenced at the surface of the insulating bulk. No transport studies exist to verify the relation between the valence transition at the surface and any associated change in electrical conductivity. This makes $\mathrm{YbIr_3Si_7}$ the first system where such correlations are identified, and the first Kondo system to exhibit enhanced Kondo conductivity due to the surface valence transition.

IV. CONCLUSIONS

$\mathrm{YbIr_3Si_7}$ shows a remarkable portfolio of physical properties that makes it unique among known Kondo systems: the "exhausted" Kondo insulating behavior is accompanied by long-range AFM order, large CEF anisotropy, and conductive surface states. This provides a complex energy landscape to explore a variety of quantum interactions and their interplay with surface properties. PES and ARPES measurements confirm the valence transition from magnetic (Yb^{3+}) in the bulk, to nonmagnetic (Yb^{2+}) on the surface, indicating a shift of the chemical potential. Within the picture of a small number of carriers, this results in an insulating behavior in the bulk, but metallic behavior at the surface.

ACKNOWLEDGMENTS

We are grateful for fruitful discussions with B. Rai, T. McQueen, N. Caroca-Canales, C. Geibel, P. Coleman, I. S. Elfimov, and L. Balicas. M.S., A.H., C.L.H., and E.M. acknowledge support from the Robert A. Welch Foundation under Grant No. C-2114. L.Q. and E.M. were also supported in part by the U.S. DOE, Grant No. BES DE-SC0019503. Research at PARADIM (Platform for the Accelerated Realization, Analysis, and Discovery of Interface Materials) was supported by the National Science Foundation Grant No. DMR-1539918. V.L. and A.H.N. were supported by the Robert A. Welch Foundation Grant No. C-1818. A.H.N. also acknowledges the support of the National Science Foundation Grant No. DMR-1350237. A portion of this work was performed at the National High Magnetic Field Laboratory, which is supported by the National Science Foundation Cooperative Agreement No. DMR-1644779, the State of Florida, and the U.S. Department of Energy. The use of the EPMA facility in the Department of Earth Science, Rice University is kindly acknowledged. K.R.L., P.D.S., and J.C.E. would like to acknowledge the support of the Jean Perkins Foundation, Florida State University, and Los Alamos National Laboratory. A.B.P. thanks the Indo-US Science and Technology Forum (IUSSTF) for financial support in the form of a postdoctoral fellowship. C.A.H. gratefully acknowledges financial support from the Engineering and Physical Sciences Research Council (UK) via Grant No. EP/R031924/1. He also thanks Rice University for its hospitality during a four-month visiting professorship, where some of this work was carried out. This research was undertaken thanks in part to funding from the Max Planck-UBC-UTokyo Centre for Quantum Materials and the Canada First Research Excellence Fund, Quantum Materials and Future Technologies Program, in addition to the Natural Sciences and Engineering Research Council of Canada (NSERC); the Canada Research Chairs Program (A.D.); Canada Foundation for Innovation (CFI); British Columbia Knowledge Development Fund (BCKDF); and the CIFAR Quantum Materials Program. Part of the research described in this paper was performed at the Canadian Light Source, a national research facility of the University of Saskatchewan, which is supported by CFI, NSERC, the National Research Council (NRC), the Canadian Institutes of Health Research (CIHR), the Government of Saskatchewan, and the University of Saskatchewan. The high-energy bulk-sensitive photoemission experiments in Japan and Taiwan were supported by the Max Planck-POSTECH-Hsinchu Center for Complex Phase Materials.

APPENDIX A: CRYSTAL GROWTH AND CRYSTALLOGRAPHY

Single crystals of $YbIr_3Si_7$ were grown via the laser pedestal technique using a Laser Diode Floating Zone (LDFZ) furnace (Crystal Systems Inc FD-FZ-5-200-VPO-PC) with 5 × 200 W GaAs lasers (976 nm) as the heat source. A polycrystalline feed rod precursor was made by arc-melting stoichiometric amounts of elemental Yb, Ir, and Si under a partial pressure of Ar. The arc-melted polycrystalline feed rod was mounted onto the lower shaft of the LDFZ furnace, and a nickel chromium (NiCr) wire was mounted onto the upper shaft above the feed rod. The tip of this rod was observed to melt ∼35% of the laser power in an Ar atmosphere of 6 bar. A floating zone was then formed by dipping the NiCr wire into the melt and then pulling the wire upward until $YbIr_3Si_7$ was observed to seed onto the wire (hereafter “seed”) (see Fig. 5). Following the initial seeding process, the lasers were held in a fixed position and both the feed and seed were translated upwards. Successive optimizations yielded final parameters of 1 mm/h feed rate, 6 mm/h seed rate, and 10 and 15.3 rpm rotation rates for counter-rotating feed and seed, respectively.

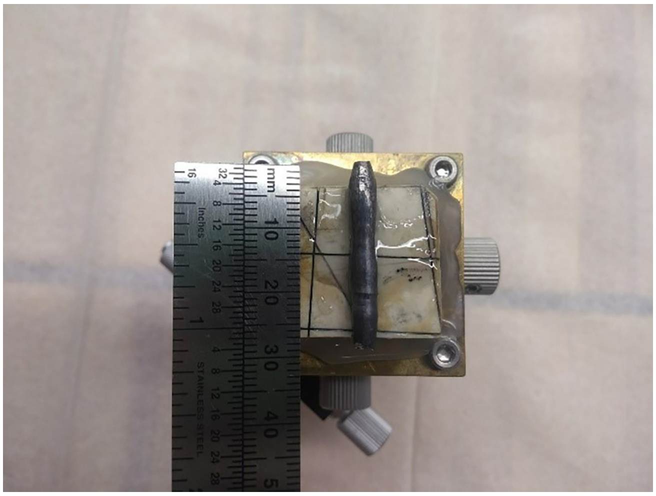

FIG. 5. Single crystal of $YbIr_3Si_7$ grown in a tilting laser diode optical floating zone furnace and mounted onto a three-axis goniometer.

Backscattering x-ray Laue diffraction was used to orient all single crystals along [100] and [001] in the equivalent hexagonal unit cell setting. Each crystal was mounted onto a three-axis goniometer, and the goniometer was placed onto the stage of a MWL101 real-time back-reflection Laue camera system from Multiwire Laboratories, Ltd. All images were collected using an applied voltage of 10 kV and current of 10 mA to the tungsten x-ray source. Total counting times for all images varied but did not exceed 5 min.

Like the polycrystalline precursor for $YbIr_3Si_7$, the nonmagnetic analog $LuIr_3Si_7$ was arc-melted into a polycrystalline bead using stoichiometric amounts of elemental Lu, Ir, and Si under a partial pressure of argon. The rhombohedral $R\text{-}3c$ space group was confirmed in both compounds using powder x-ray diffraction refinement. Additionally, single-crystal x-ray diffraction refinement was used to confirm the $R\text{-}3c$ space group and full occupancies of the crystallographic sites in $YbIr_3Si_7$. Powder x-ray diffraction measurements were performed at ambient temperature using a Bruker D8 Advance diffractometer with Cu $K\alpha$ radiation (see Fig. 6). Rietveld refinement was done using the TOPAS software package. Single-crystal x-ray diffraction was conducted using a Rigaku SCX mini diffractometer with Mo $K\alpha$ radiation. Integration of raw frame data was done using CRYSTALCLEAR 2.0. Refinement of the diffraction data was performed using XPREP and SHELXTL software packages.

Electron probe microanalysis (EPMA) was performed to obtain quantitative analysis of the Yb-Ir-Si and Lu-Ir-Si

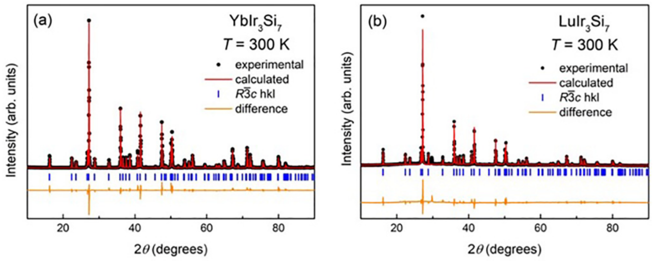

FIG. 6. Powder x-ray diffraction and refinement of $YbIr_3Si_7$ and $LuIr_3Si_7$.

phases using wavelength dispersive spectrometry (WDS). The compositions were shown to be $Yb_{0.99(1)}Ir_{3.00(2)}Si_{7.01(2)}$ and $Lu_{1.02(3)}Ir_{3.04(4)}Si_{6.95(6)}$. The data were acquired at the EPMA laboratory, Earth Science Department, Rice University, using a JEOL JXA 8530F Hyperprobe equipped with a field emission (Schottky) emitter and five WDS spectrometers. The analytical conditions used were 15 kV accelerating voltage, 50 nA beam current, 300 nm beam diameter, and counting times of 10 s per peak and 5 s per each lower and upper background, respectively. The standards used for element calibration were synthetic metals (Si metal and Ir metal) for Si and Ir, respectively, and REE2 glass8 for Lu and Yb. Both Ir and Yb were concomitantly analyzed on two different spectrometers using two types of diffracting crystals (LiF and LiFH for Ir and PET and PETL for Yb) in order to improve the x-ray statistics and increase the accuracy of the analysis. LiFH and PETL diffracting crystals have much higher sensibility (three to four times higher x-ray intensities) compared to LiF and PET crystals. The PhiRoZ matrix correction was employed for quantification.

APPENDIX B: THERMODYNAMIC AND TRANSPORT PROPERTIES

Resistivity and specific-heat measurements were performed in a Quantum Design (QD) physical property measurement system (PPMS) equipped with a ^{3}He insert. Temperature-dependent ac resistivity measurements were performed using $i = 0.05$ mA ($i = 0.1$ mA above 50 K) and $f = 35.54$ Hz for a duration of 3 s. Resistivity measurements on different thicknesses of a sample were conducted on the same sample repeatedly thinned using mechanical polishing with the leads reapplied before each measurement. The crystal dimensions d, w, and L were measured using a digital microscope and Moticam 3.0 measurement software. For each measurement, $w = 1.063(53)$ mm. Dimensions d and L for each measurement are given in Table I.

TABLE I. Crystallographic parameters of $YbIr_3Si_7$ single crystals at $T = 173$ K (R-3c).

Formula	$YbIr_3Si_7$
a (Å)	7.5562(3)
c (Å)	20.0662(11)
V (Å^3)	992.21(9)
Crystal dimensions (mm^3)	0.1 × 0.07 × 0.07
θ range (deg)	3.7–30.6
Extinction coefficient	0.00072(2)
Absorption coefficient (mm^{-1})	75.329
Measured reflections	7570
Independent reflections	377
R_{int}	0.0807
Goodness-of-fit on F^2	1.053
$R_1(F)$ for $F_o^2 \geqslant 2\sigma(F_o^2)$[a]	0.0220
$wR_2(F_o^2)$[b]	0.0379

[a] $R_1 = \sum ||F_o| - |F_c|| / \sum |F_o|$.

[b] $wR_2 = [\sum[w(F_o^2 - F_c^2)^2] / \sum[w(F_o^2)^2]]^{\frac{1}{2}}$.

TABLE II. Dimensions d and L for the sample used in thickness-dependent resistivity measurements.

d (mm)	L (mm)
0.723(36)	1.413(71)
0.588(29)	1.250(63)
0.453(23)	1.140(57)
0.260(13)	0.455(23)
0.175(18)	0.655(33)
0.110(11)	0.765(38)
0.077(8)	0.273(14)

Additional resistivity measurements performed up to 14 T were done using a QD DynaCool Physical Properties Measurement System equipped with a dilution refrigerator. The electrical transport option for resistivity was performed us-

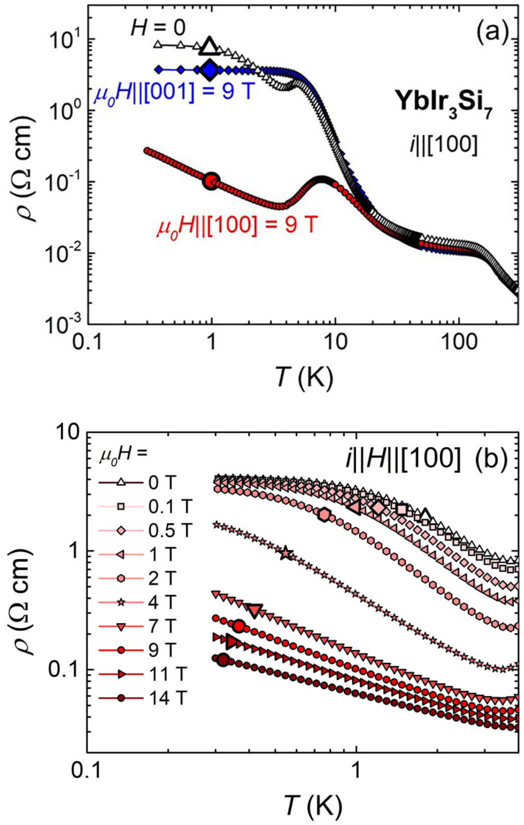

FIG. 7. (a) Log-log plot of the temperature-dependent resistivity in $H = 0$ (triangles) and in applied magnetic field $\mu_0H = 9$ T, $H \parallel [100]$ (circles), and $H \parallel [001]$ (diamonds), and (b) $H \parallel [100]$ from 0 to 14 T.

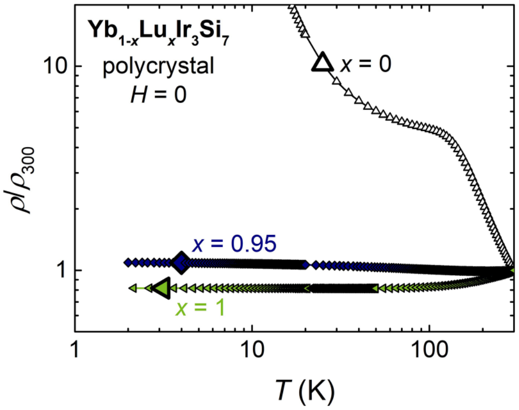

FIG. 8. Scaled resistivity measurements of the doped $Yb_{1-x}Lu_xIr_3Si_7$ polycrystalline samples for $x = 0$ (open triangles), $x = 0.95$ (diamonds), and $x = 1$ (full triangles).

ing $i = 0.1$–1 mA, $f = 18.3$ Hz, and an averaging time of 2.3 s. Specific-heat measurements were performed using an adiabatic relaxation method. A QD magnetic properties measurement system was used to perform dc magnetic susceptibility measurements up to 400 K. High-temperature magnetic susceptibility measurements were carried out on a QD PPMS equipped with the VSM oven option. The measurements covered a temperature range from 300 to 1000 K. The system calibration was confirmed both before and after the measurements using a palladium calibration standard, the system showing a repeatability of better than 0.2%. Each sample was measured at least three times with each run agreeing within the noise floor of the system.

For the neutron diffraction measurements, the sample was loaded into a liquid-helium cryostat with a base temperature of 1.5 K. To search for magnetic scattering, the high intensity-coarse resolution BT-7 spectrometer was employed in two-axis mode, with a fixed initial neutron energy of 14.7 meV (wavelength 2.359 Å) and collimator (full width at half-maximum) configuration open–PG(002) monochromator–80′–sample–80′ radial-collimator–position-sensitive detector [25]. The refinements were determined by the Rietveld method with the FULLPROF suite [26].

Figure 7 shows details of the electrical resistivity $\rho(T)$ on a log-log scale for (a) $\mu_0 H = 0$ (triangles), 9 T, and $H \parallel [100]$ (circles) and $H \parallel [001]$ (diamonds), and (b) $i \parallel H \parallel [100]$, with applied field values up to 14 T. The preliminary anisotropic $\rho(T)$ data [Fig. 7(a)] point to a qualitative change of the temperature dependence with increasing field. Indeed, the applied magnetic field [Fig. 7(b)] changes the temperature dependence from $-\ln T$ ($H = 0$, open triangles) to power law $-T^\alpha$ above $\mu_0 H \sim 7$ T. In a Kondo screening scenario, it can indeed be expected that the $\ln T$ divergence of the resistivity at low T changes to a power law with band polarization in an applied magnetic field.

Nonmagnetic Lu doping in $YbIr_3Si_7$ was used in an attempt to characterize the ~100 K inflection in the $H = 0$ $\rho(T)$ data. Single-ion CEF effects would be expected to scale with the number of magnetic Yb ions $(1 - x)$ in $Yb_{1-x}Lu_xIr_3Si_7$. Since the resistivity inflection has disappeared in the highly diluted $x = 0.95$ sample (Fig. 8, diamonds), it is unlikely due to CEF effects, rendering the onset of Kondo correlations the most likely scenario. Indeed, inelastic neutron-scattering measurements shown in Fig. 9 confirm that the lowest CEF level is at 19 meV, or ~200 K, with no low-energy crystal-field excitations. Furthermore, anisotropic inverse magnetic susceptibility data shown in Fig. 10 indicate that no deviations from the Curie-Weiss law are observed in the average inverse magnetic susceptibility (solid line, Fig. 10) up to 600 K.

Figure 11 shows the temperature-dependent specific heat C_P (a) and magnetic susceptibility M/H (b) measured in different fields, as well as an example of an $M(H)$ isotherm [(c), $T = 2.6$ K] for $H \parallel [001]$. Increasing field moves the antiferromagnetic transition to lower temperatures T_N [full triangle, (a)]. However, above $\mu_0 H = 2.5$ T, the C_P peak defines the

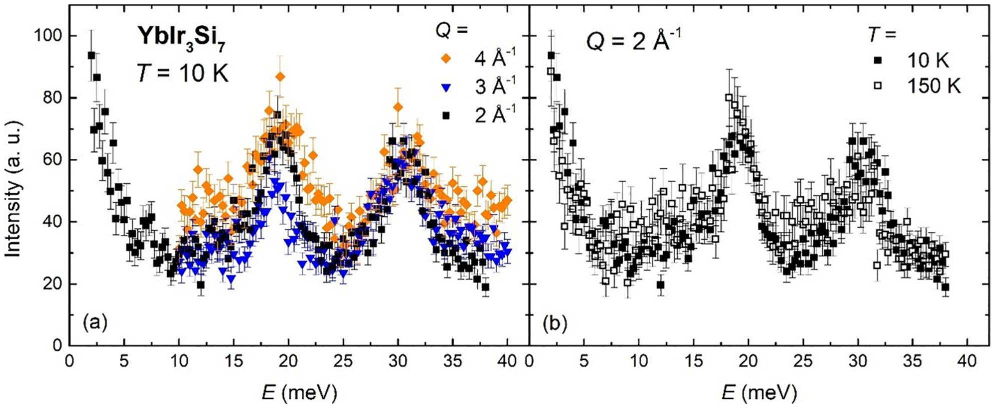

FIG. 9. Inelastic neutron scattering data taken on BT-7 using a pyrolytic graphite (PG) monochromator, analyzer, a fixed final energy of 14.7 meV with PG filters, an 80 full width at half-maximum radial collimator, and a horizontal focusing analyzer. The collimations before and after the monochromator were OPEN (≈1.5°) and 50′, respectively. The Q dependence of the scattering (left) indicates that the signal for both peaks decreases with increasing Q as expected for magnetic scattering, after considering that the background increases with Q, while phonon scattering would be expected to increase approximately as $Q2$. The data on the right show that there is very little change in the scattering in going from 10 K (above the ordering temperature) to 150 K, which demonstrates that there are no "hidden" low-energy crystal-field levels (with small matrix elements too small to be observed), indicating that the lowest CEF level is at 19 meV.

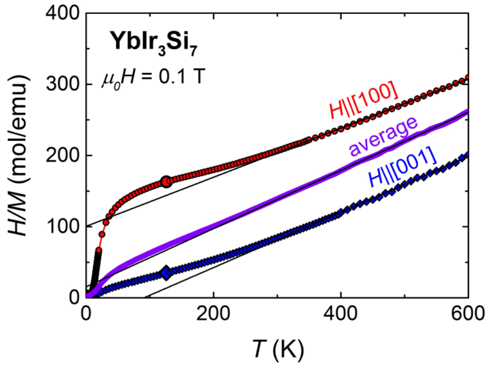

FIG. 10. Anisotropic inverse magnetic susceptibility measurements (symbols) and calculated polycrystalline average H/M_{ave} (line) with $M_{\mathrm{ave}} = 2/3M_{100} + 1/3M_{001}$. Solid black lines are linear fits above 350 K, providing evidence of Curie-Weiss behavior.

emergence of a possible phase boundary, albeit broad, as T moves to slightly larger values as μ_0H increases up to 9 T (open side triangle). The AFM phase boundary is also marked by a peak in $M(T)$ [symbols, (b)], with T_N determined from the peak in $d(MT)/dT$ (open square) and the metamagnetic transition best evidenced as the maximum [full square, (c)] in the derivative dM/dH (line). The resulting phase diagram is shown in Fig. 11(d). An as-of-yet unexplained broad maximum in $M(T)$ [Fig. 11(b), large circle] is depicted as a crossover (gray line) in the phase diagram.

The complex field dependence of the thermodynamic measurements motivated an investigation of the field dependence of the magnetoresistance. Large longitudinal magnetoresistance (MR) is registered in YbIr$_3$Si$_7$ (Fig. 12). At $T =$ 10 K ($T > T_{\mathrm{N}}$, open circles), a moderately large MR (14 T) $\sim -53\%$ was measured with $i \parallel H \parallel [100]$. For temperatures below T_N (full symbols), the negative MR increases to a maximum of $\sim -95\%$ and plateaus above 8 T. This large, negative MR below the ordering temperature is similar to that of the magnetic Kondo insulator UFe$_4$P$_{12}$, where the MR approaches -90% near the ordering temperature [27], attributed to the delocalization of the conduction electrons by disturbing the Kondo screening with an applied magnetic field. SmB$_6$ reaches a similarly large, negative MR, albeit at a much higher applied field of 86 T when the hybridization gap is closed [28]. This field value is nearly an order of magnitude larger than in YbIr$_3$Si$_7$, consistent with a Kondo temperature of ~80 K in the former [29], an order of magnitude larger than T_{K} in the present compound.

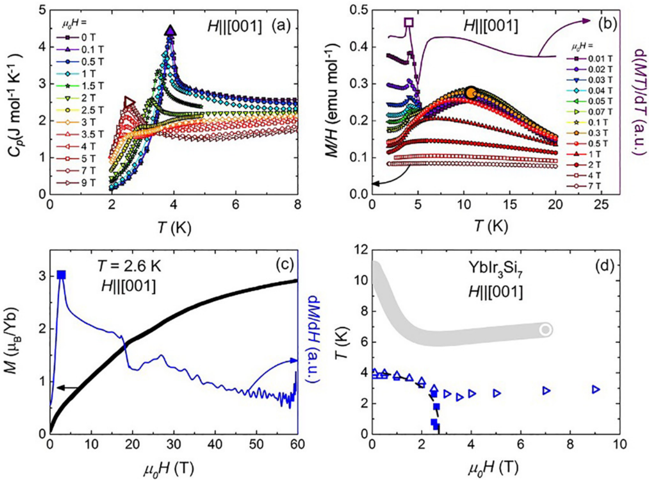

FIG. 11. Temperature-dependent (a) specific heat C_{p} and (b) magnetic susceptibility M/H in applied magnetic fields up to 14 T for $H \parallel [001]$. (c) $T = 2.6$ K magnetization isotherm $M(H)$ (black line, left axis) and the derivative dM/dH (blue line, right axis); large square: low-H metamagnetic transition. (d) T-H phase diagram for $H \parallel [001]$ derived from peaks in C_{P} and $M(T, H)$ data; up-triangles: $\mu_0H = 0$–2.5 T; right triangle: $\mu_0H = 3$–9 T; squares: $d(MT)/dT$ (open) and dM/dH (full); gray line: broad peak in M/H, likely a crossover.

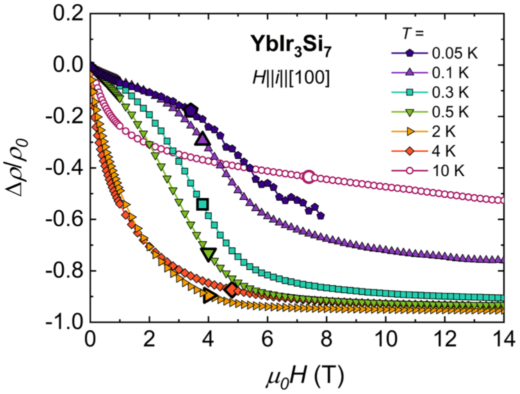

FIG. 12. Longitudinal magnetoresistance $i \parallel H \parallel [100]$ below (full symbols) and above (open symbols) T_{N}.

APPENDIX C: BAND-STRUCTURE CALCULATIONS

To obtain an insight into the electronic properties of YbIr$_3$Si$_7$, we have performed first-principles density functional theory (DFT) calculations using the generalized gradient approximation for the exchange-correlation functional following Perdew, Burke, and Ernzerhof (PBE) [30]. The full-potential linearized augmented plane-wave (LAPW) method was used, as implemented in the WIEN2K package [31], with the scalar spin-orbit coupling included in the calculation. We have performed the electronic structure in the paramagnetic (PM) and the antiferromagnetically (AFM) ordered ground state of YbIr$_3$Si$_7$, as determined from the neutron scattering (see Fig. 4 in the main text). The resulting band structure in the paramagnetic state is shown in Fig. 13(a), plotted along the high-symmetry lines in the Brillouin zone (BZ), with the radius of the circles reflecting the f-electron contribution to the respective Bloch band. In an attempt to capture the effect of strong correlations on the f-orbitals, we have performed the DFT+U calculations in the AFM state, with the Hubbard $U = 4$ eV on Yb ions. This results in one f-band at the chemical potential, shown in Fig. 13(b), which is split from the other six f-bands that now lie about 4 eV below (not shown).

As Fig. 13 shows, the nearly flat Yb 4f band (light green in the center of the plot) hybridizes with the dispersive conduction electron band. Intriguingly, there is another conduction

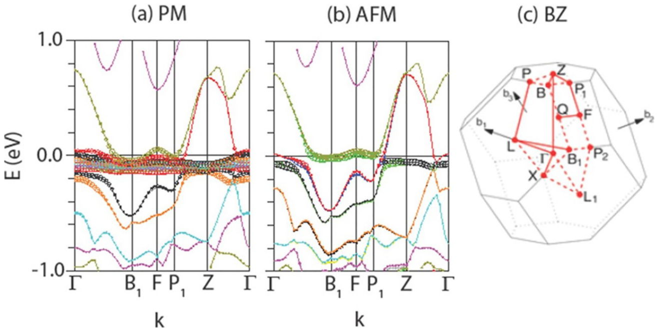

FIG. 13. First principles DFT band structure of $\mathrm{YbIr_3Si_7}$ in (a) PM and (b) AFM states plotted along the high-symmetry lines in the Brillouin zone shown in panel (c). The results in panel (b) were obtained within the DFT+U method ($U = 4$ eV) to approximately capture the effect of electron correlations on Yb ion.

band [inverted parabola centered around the Z point, shown in red in Figs. 13(a) and 13(b)], which appears not to hybridize with the f band. As a result, there is a nonvanishing electron density of states at the chemical potential in both the PM and AFM states. Based on these results, DFT would predict $\mathrm{YbIr_3Si_7}$ to be a metal, contrary to the insulating behavior of the bulk resistivity reported in Fig. 1 in the main text. The Kondo hybridization, central to understanding this behavior, is a many-body effect not captured by the single-particle DFT calculations. Other, nonperturbative techniques are desirable in order to understand this effect. However, they are beyond the scope of the present work and are left for an upcoming study.

APPENDIX D: PHOTOELECTRON SPECTROSCOPY

Photoemission has been used to determine the Yb valence in $\mathrm{YbIr_3Si_7}$. The $3d$ core-level photoemission spectrum of $\mathrm{YbIr_3Si_7}$ was measured using 9.8 keV photons at a temperature of 80 K. This experiment has been carried out at the Taiwan undulator beamline BL12XU at SPring-8, Japan. The use of hard x-rays in PES (HAXPES) provides a large probing depth and ensures that the signal is representative for the bulk material. We have also carried out PES measurements to study the valence band. The soft x-ray experiments were performed at Beamline TPS45A of the NSRRC in Taiwan, using photons with $h\nu = 858$ eV for bulk sensitivity and with an energy resolution of 80 meV. The measurement temperature was 15 K. Low-energy PES and ARPES experiments have been performed at the QMSC beamline at the Canadian Light Source. The freshly cleaved sample was maintained at a temperature of 13 K using a photon energy of 182 eV for PES and 88 eV for ARPES data.

---

[1] B. K. Rai, M. Stavinoha, J. Banda, D. Hafner, K. A. Benavides, D. A. Sokolov, J. Y. Chan, M. Brando, C.-L. Huang, and E. Morosan, Phys. Rev. B **99**, 121109(R) (2019).
[2] B. K. Rai, S. Chikara, X. Ding, I. W. H. Oswald, R. Schönemann, V. Loganathan, A. M. Hallas, H. B. Cao, M. Stavinoha, T. Chen, H. Man, S. Carr, J. Singleton, V. Zapf, K. A. Benavides, J. Y. Chan, Q. R. Zhang, D. Rhodes, Y. C. Chiu, L. Balicas *et al.*, Phys. Rev. X **8**, 041047 (2018).
[3] D. Hafner, B. K. Rai, J. Banda, K. Kliemt, C. Krellner, J. Sichelschmidt, E. Morosan, C. Geibel, and M. Brando, Phys. Rev. B **99**, 201109(R) (2019).
[4] C. J. P. S. Tanuma and D. R. Penn, Surf. Interface Anal. **43**, 689 (2011).
[5] S. Suga, A. Sekiyama, S. Imada, J. Yamaguchi, A. Shigemoto, A. Irizawa, K. Yoshimura, M. Yabashi, K. Tamasaku, A. Higashiya, and T. Ishikawa, J. Phys. Soc. Jpn. **78**, 074704 (2009).
[6] Y. Utsumi, H. Sato, K. Tobimatsu, H. Maso, K. Hiraoka, K. Kojima, K. Mimura, S. Ueda, Y. Yamashita, H. Yoshikawa, K. Kobayashi, K. Shimada, H. Namatame, and M. Taniguchi, J. Electron Spectrosc. Relat. Phenom. **184**, 203 (2011).
[7] N. E. Bickers, D. L. Cox, and J. W. Wilkins, Phys. Rev. B **36**, 2036 (1987).
[8] L. H. Tjeng, S.-J. Oh, E.-J. Cho, H.-J. Lin, C. T. Chen, G.-H. Gweon, J.-H. Park, J. W. Allen, T. Suzuki, M. S. Makivić, and D. L. Cox, Phys. Rev. Lett. **71**, 1419 (1993).
[9] G. K. Wertheim, J. H. Wernick, and G. Crecelius, Phys. Rev. B **18**, 875 (1978).
[10] S. Alvarado, M. Campagna, and W. Gudat, J. Electron Spectrosc. Relat. Phenom. **18**, 43 (1980).
[11] B. Johansson, Phys. Rev. B **19**, 6615 (1979).
[12] O. Gunnarsson and K. Schönhammer, Phys. Rev. B **28**, 4315 (1983).
[13] S. Kitagawa, T. Kobayashi, F. Hori, K. Ishida, A. H. Nevidomskyy, L. Qian, and E. Morosan, Phys. Rev. B **106**, L100405 (2022).
[14] D. Meyer and W. Nolting, Phys. Rev. B **61**, 13465 (2000).
[15] L. Qian, S. Lei, B. K. Rai, C. L. Huang, A. M. Hallas, G. T. McCandless, J. Y. Chan, and E. Morosan, Phys. Rev. Mater. **5**, 094416 (2021).
[16] L. Qian and E. Morosan (unpublished).
[17] L. Qian, K. Neubauer, J. Miller, Y. Gao, J. Murley, S. Chi, S. Lei, P. Dai, and E. Morosan, Phys. Rev. B (to be published).
[18] S. Suzuki, T. Tomita, Y. Shimura, K. Kuga, Y. Matsumoto, and S. Nakatsuji, J. Phys.: Conf. Ser. **683**, 012009 (2016).
[19] M. Matsunami, H. Okamura, T. Nanba, T. Suemitsu, T. Yoshino, T. Takabatake, and Y. Isikawa, J. Phys. Soc. Jpn. **71**, 291 (2002).
[20] J. Arvanitidis, K. Papagelis, S. Margadonna, K. Prassides, and A. N. Fitch, Nature (London) **425**, 599 (2003).
[21] A. Mitsuda, H. Wada, R. Masuda, S. Kitao, M. Seto, Y. Yoda, and H. Kobayashi, J. Phys. Soc. Jpn. **89**, 104703 (2020).
[22] K. Matsubayashi, T. Hirayama, T. Yamashita, S. Ohara, N. Kawamura, M. Mizumaki, N. Ishimatsu, S. Watanabe, K. Kitagawa, and Y. Uwatoko, Phys. Rev. Lett. **114**, 086401 (2015).

[23] E.-J. Cho and S.-J. Oh, Phys. Rev. B **59**, R15613 (1999).

[24] V. N. Antonov, A. N. Yaresko, A. Y. Perlov, P. Thalmeier, P. Fulde, P. M. Oppeneer, and H. Eschrig, Phys. Rev. B **58**, 9752 (1998).

[25] J. W. Lynn, S. C. Y. Chen, Y. Zhao, S. Chi, W. Ratcliff, B. G. Ueland, and R. W. Erwin, J. Res. Natl. Inst. Stand. Technol. **117**, 60 (2012).

[26] J. Rodríguez-Carvajal, Phys. B: Condens. Matter **192**, 55 (1993).

[27] M. Torikachvili, C. Rossel, M. McElfresh, M. Maple, R. Guertin, and G. Meisner, J. Magn. Magn. Mater. **54-57**, 365 (1986).

[28] J. Cooley, C. Mielke, W. Hults, J. Goettee, M. Honold, R. Modler, A. Lacerda, D. Rickel, and J. Smith, J. Supercond. **12**, 171 (1999).

[29] W. A. Phelan, S. M. Koohpayeh, P. Cottingham, J. W. Freeland, J. C. Leiner, C. L. Broholm, and T. M. McQueen, Phys. Rev. X **4**, 031012 (2014).

[30] J. P. Perdew, K. Burke, and M. Ernzerhof, Phys. Rev. Lett. **77**, 3865 (1996).

[31] P. Blaha, K. Schwarz, G. Madsen, D. Kvasnicka, and J. Luitz, A study by ab-initio calculation of structural and electronic properties of semiconductor nanostructures based on ZnSe, Vienna University of Technology (Vienna) (2001).